A publishing partnership Rotational Line Emission from Water in Protoplanetary Disks

Meijerink, R.; Poelman, D. R.; Spaans, M.; Tielens, A. G. G. M.; Glassgold, A. E.

Published in:
Astrophysical Journal Letters

DOI:
10.1086/595726

The Astrophysical Journal, 689: L57–L60, 2008 December 10

ROTATIONAL LINE EMISSION FROM WATER IN PROTOPLANETARY DISKS

R. Meijerink,[1] D. R. Poelman,[2] M. Spaans,[3] A. G. G. M. Tielens,[4,3] and A. E. Glassgold[1]

Received 2008 June 18; accepted 2008 October 16; published 2008 November 6

ABSTRACT

Circumstellar disks provide the material reservoir for the growth of young stars and for planet formation. We combine a high-level radiative transfer program with a thermal-chemical model of a typical T Tauri star disk to investigate the diagnostic potential of the far-infrared lines of water for probing disk structure. We discuss the observability of pure rotational H_2O lines with the *Herschel Space Observatory*, specifically the residual gas where water is mainly frozen out. We find that measuring both the line profile of the ground 1_{10}–1_{01} ortho-H_2O transition and the ratio of this line to the 3_{12}–3_{03} and 2_{21}–2_{12} lines can provide information on the gas-phase water between 5 and 100 AU, but not on the snow line which is expected to occur at smaller radii.

Subject headings: accretion, accretion disks — infrared: stars — planetary systems: protoplanetary disks — radiative transfer — stars: pre–main-sequence — X-rays: stars

1. INTRODUCTION

The radius where volatiles sublimate in a protoplanetary disk plays an important role in planet formation. Of particular interest is water and the place where it freezes out onto grains is called the *snow line* (Hayashi 1981). The sublimation temperature for water is $T \sim 110$–170 K, depending on the water vapor pressure (cf. Fraser et al. 2001; Podolak & Zucker 2004). At radii larger than the snow line, planetesimals and protoplanets may be hydrated. Hayashi (1981) found that the snow line is located at ~2.7 AU from the Sun in our solar system. However, the position can be different for a T Tauri star. Its location depends on the evolutionary phase of the disk and varies from 0.7 to 10 AU (Sasselov & Lecar 2000; Lecar et al. 2006; Garaud & Lin 2007).

Gas-phase water is expected to be abundant between the water-ice sublimation temperature $T \sim 110$–170 K and the dissociation temperature $T \sim 2500$ K. Its rich spectrum covers almost all wavelength bands. Using the near-infrared lines near 2.3μm, Carr et al. (2004) and Thi & Bik (2005) found warm H_2O in protoplanetary disks at temperatures $T > 1200$ K and radii $R < 0.4$ AU, and Carr & Najita (2008) and Salyk et al. (2008) have detected mid-infrared water lines with *Spitzer*. The far-infrared spectrometers aboard the *Herschel* space telescope will allow studies of the pure rotational H_2O transitions characteristic of gas temperatures of $T \gtrsim 60$ K. Because gas-phase H_2O requires warm conditions ($T \gtrsim 200$ K) it is expected to be abundant at small radii and thus perhaps not observable with the *Herschel* spectrometers. However, temperatures appropriate to both the occurrence and detection of H_2O are present over a wide range of radii because stellar radiation heats the disk atmosphere. Moreover, as we will show, several lines of H_2O can be detected by *Herschel* at very low abundances close to the midplane where the bulk of the water is frozen. Detection of these lines will complement measurements of the near- and mid-infrared water lines.

[1] Astronomy Department, University of California, Berkeley, CA 94720; rowin@gps.caltech.edu.

[2] School of Physics and Astronomy, University of St Andrews, North Haugh, St Andrews KY16 9SS, Scotland.

[3] Kapteyn Astronomical Institute, P.O. Box 800, 9700 AV Groningen, Netherlands.

[4] NASA Ames Research Center, MS 245-3, Moffett Field, CA 94035.

2. MODELS

The calculation is done as follows: (1) We use an X-ray irradiated disk code to calculate the temperature structure and molecular abundances for a generic T Tauri disk. (2) The results are input into a multizone radiative transfer code that calculates the excitation of H_2O lines. (3) A ray-tracing code is used to obtain line fluxes and line shapes.

(1) The thermal-chemical structure of the disk is calculated with the code described by Glassgold et al. (2004) with minor corrections and updates (Meijerink et al. 2008). The disk is illuminated by stellar X-rays with a thermal spectrum with temperature $T_X = 1$ keV and luminosity $L_X = 2 \times 10^{30}$ erg s^{-1}. In regions where the X-rays are strongly attenuated, the disk is ionized by the decay products of ^{26}Al at a rate $\zeta_{26} = 4 \times 10^{-19}$ s^{-1}. The density structure is given by the generic T Tauri disk model (Paola d'Alessio, private communication) with accretion rate $\dot{M} = 10^{-8}\ M_\odot$ yr^{-1} and stellar parameters $M_* = 0.5\ M_\odot$, $R_* = 2\ R_\odot$, and $T_* = 4000$ K. The disk is flared, and the density varies continuously from $R = 0.028$ to >500 AU. The model density does not include modifications such as holes, gaps, and rims suggested, for example, by the spectral energy distributions measured with *Spitzer* (e.g., Dullemond et al. 2007). The adopted model has a power-law grain size distribution with index −3.5 and minimum and maximum grain sizes of 0.005 and 1000 μm, resulting in a geometric mean grain size, $a_g = 2.24$ μm, which controls the thermal coupling between dust and gas.

The D'Alessio et al. (1999, 2001) dust temperature involves a balance between heating by viscous dissipation, FUV/optical/IR radiation, cosmic rays, and cooling by IR radiation. Our gas temperature is determined by heating by penetrating X-rays, gas-grain collisions and cooling by atomic and molecular lines. The gas thermal model relies solely on X-ray irradiation in contrast to UV irradiation models by Jonkheid et al. (2004, 2007), Kamp & Dullemond (2004), and Nomura et al. (2007) (who also include X-rays). UV irradiation, however, plays no role in the regions where the submillimeter H_2O emission is produced. The numerical approach is "1+1D," i.e., the vertical thermal and chemical structure is calculated independently at 45 radial points. However, the X-ray attenuation is calculated along the line of sight to the star. The photons can only escape in the vertical direction, a reasonable approximation, since the opacities in the radial direction are so much larger.

The chemistry is steady state, entirely gas phase, and in-

cludes only carbon and oxygen bearing species. It does not treat freezeout of H_2O in detail, but we expect that freezeout cannot be 100% efficient. Incomplete freezeout has been observed by *ISO* (Boonman et al. 2003), and Davis (2007) has modeled freezeout in irradiated accretion disks. In order to treat the freezeout of water, we assume a fixed gas-phase water abundance, $x_f(H_2O) = 10^{-8}$ or $x_f(H_2O) = 10^{-10}$, in regions where most of the water is expected to freeze out on grains, i.e., where the gas temperature satisfies the condition $T < 110$ K. Where the model gas-phase abundance is lower, we adopt the calculated abundance. A more realistic treatment of water freezeout involves treating poorly understood physical processes, including growth and settling of dust grains, chemistry on grain surfaces, adsorption and desorption, and mixing. We are developing an improved thermal-chemical disk model that will address these issues. The present model is allows us to isolate the chemical effects of freezeout and the effects of grain growth and settling in a simple albeit preliminary way.

(2) The critical densities of the lines of interest are typically high, in the range $n_{crit} \sim 10^8$–10^{10} cm^{-3}. The water fractional abundance becomes significant at perpendicular column densities $N_H > (2–5) \times 10^{21}$ cm^{-2} (Fig. 1), and excitation can be subthermal, especially at large radii ($R > 10$–20 AU). Thus local thermodynamic equilibrium is not always a good approximation, and a full radiation transfer calculation is required.

We calculate the level populations of H_2O using the multi-zone escape probability method β3D described by Poelman & Spaans (2005, 2006). We assume Keplerian rotation for a stellar mass $M_* = 0.5\ M_\odot$ and turbulent velocities $\delta v = 0.5$, and 2.0 km s^{-1}. The medium is divided into a large number of grid cells, each with calculated values of the volumetric hydrogen density, the temperatures of gas and dust, and the H_2O abundance. The connection of every grid cell with all the others enables us to solve locally the equations of statistical equilibrium taking into account global information for the entire disk. Radiative and collisional excitation and de-excitation by electrons and atomic and molecular hydrogen, and dust pumping are included, using data from Faure & Josselin (2008) and the Leiden Atomic and Molecular Database (LAMDA; Schöier et al. 2005). We adopt the dust opacities from D'Alessio et al. (2001). Although the radiative transfer code can deal with three dimensions, we only consider 1D slabs here.

(3) We compute line profiles for inclinations from 0° to 90° with the sky brightness distribution program SKY, part of the RATRAN code (Hogerheijde & van der Tak 2000). We use the two-dimensional cylindrically symmetric version of SKY, and the level populations, densities, and molecular abundances at each radius are combined and rebinned into a single grid. The dynamical ranges of the physical and chemical properties are large in the vertical direction and we use 400 cells in this direction.

3. RESULTS AND DISCUSSION

Figure 1 shows the gas temperature and H_2O abundance for a range of radii from $R = 1$–40 AU plotted versus increasing perpendicular column density N_H. As explained in more detail in Glassgold et al. (2004) and Meijerink et al. (2008) the stellar X-rays heat the gas at the top of the atmosphere as high as $T \sim 3000$–4000 K for $R < 20$ AU. Attenuation of the X-rays for $N_H > 10^{21}$ cm^{-2} produces a drop in temperature and induces transitions from atoms (or ions) to molecules. For example, the H to H_2 transition occurs for $N_H = 10^{21}$–10^{22} cm^{-2}. The water abundance before the H to H_2 transition is small due to the efficient destruction by X-ray ionized species such as H^+ and He^+. Congruent with the H to H_2 transition, the water abundance increases steeply.

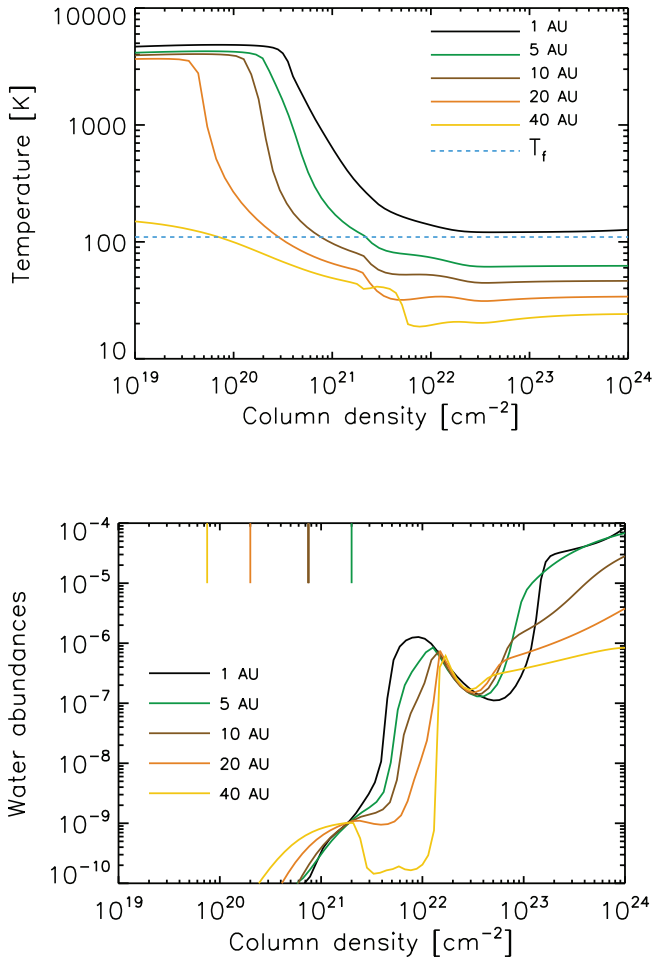

FIG. 1.—Temperature (*top*) and fractional water abundance (*bottom*) vs. perpendicular column density. The dotted blue line (*top*) shows the freezeout temperature $T_f = 110$ K. The colored tick marks at the top of the bottom panel indicate the smallest perpendicular column density for each radius where water freezes out. No freezeout occurs within $R = 1$ AU. Note the non-monotone variation of the water abundance due to gradients in the ionization rate, density, and temperature.

According to Figure 1, freezeout occurs for $R > 1$ AU and for $N_H \gtrsim 10^{19}$–10^{22} cm^{-2} depending on radius. The densities here are quite high, $n_H = 10^8$–10^{12} cm^{-3}, and the gas is thermally coupled to the dust. At even higher column densities than shown in Figure 1, the temperature increases slightly due to viscous accretion heating. Temperatures greater than $T \sim 200$ K are needed for efficient gas-phase synthesis of water by neutral radical reactions, and they are only attained at small radii $R < 0.5$ AU, where $x(H_2O) > 10^{-4}$ for $N_H > 10^{22}$–10^{23} cm^{-2}.

We have calculated line profiles and fluxes for the low-excitation H_2O transitions in the spectral range of *Herschel* Photodetector Array Camera and Spectrometer (PACS) and Heterodyne Instrument for the Far-Infrared (HIFI). The results indicate that a number of lines in the HIFI frequency bands are detectable. The PACS frequency bands are less favorable, and the following discussion is based on HIFI. Integrated fluxes are summarized in Table 1 for sources at an assumed distance of 140 pc. Initially, only the ortho 1_{10}–1_{01} and para 1_{11}–0_{00} ground-level transitions will be observed in the *Herschel* key

TABLE 1

INTEGRATED INTENSITIES $I = \int T_{MB} dv$(mK km s^{-1})[a]

		No Freezeout		$x_f = 10^{-8}$		$x_f = 10^{-10}$	
		Turbulent Velocity δv (km s^{-1})[b]					
Trans.	Freq. (GHz)	0.5	2.0	0.5	2.0	0.5	2.0
ortho-H_2O lines							
1_{10}–1_{01}	556.936	13.7	66.2	16.3	59.3	13.6	41.8
3_{12}–3_{03}	1097.37	32.7	120.9	19.1	50.6	3.9	7.0
3_{12}–2_{21}	1153.13	33.5	103.6	12.5	29.0	1.4	1.9
3_{21}–3_{12}	1162.91	27.6	94.6	12.9	32.5	2.4	4.3
2_{21}–2_{12}	1661.01	34.3	143.7	29.8	97.2	10.9	20.5
2_{12}–1_{01}	1669.90	21.1	114.2	26.6	97.0	25.5	85.5
3_{03}–2_{12}	1716.77	38.9	150.2	32.3	110.1	15.5	33.2
3_{30}–3_{21}	2196.35	25.3	98.1	11.5	27.9	2.1	3.5
4_{14}–3_{03}	2640.47	28.6	125.3	25.3	73.0	9.2	20.0
2_{12}–1_{10}	2773.97	16.1	96.2	21.4	69.1	17.0	51.0
para-H_2O lines							
2_{11}–2_{02}	752.029	27.6	108.7	21.3	62.5	4.9	7.9
2_{02}–1_{11}	987.924	39.9	138.9	29.8	102.4	10.6	17.3
1_{11}–0_{00}	1113.34	21.4	105.5	24.9	94.5	23.1	70.0
2_{20}–2_{11}	1228.80	32.7	124.5	20.7	56.9	3.9	6.0

[a] Adopting a distance $d = 140$ pc.
[b] δv is the 1/e half-width of the line profile.

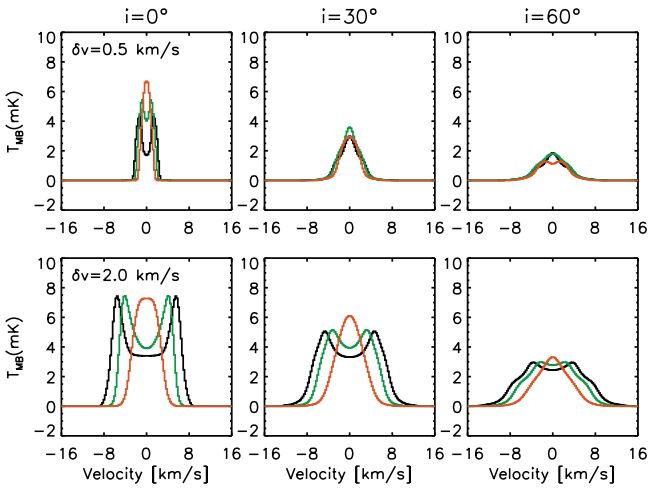

FIG. 2.—The 1_{10}–1_{01} ortho-H_2O lines with the d'Alessio opacities for inclinations of 0° (*left*), 30° (*middle*), and 60° (*right*); no freezeout (*black*), with freezeout below 110 K and abundance $x_f(H_2O) = 10^{-8}$ (*green*) and $x_f(H_2O) = 10^{-10}$ (*red*) in the freezeout zone; turbulent velocity $\delta v = 0.5$ (*top*), and 2.0 km s^{-1} (*bottom*).

program "Water in Star-forming Regions with *Herschel*" (WISH)[5] and we discuss these lines first.

The line profiles of the 556.936 GHz 1_{10}–1_{01} ortho and the 1113.34 GHz 1_{11}–0_{00} para transitions are convolved with the 38″ and 19″ *Herschel* beam sizes at these frequencies. Figure 2 shows the effects of inclination angle i, turbulent velocity δv, and incomplete freezeout on the profile of the 1_{10}–1_{01} ortho transition. The integrated intensities for the models shown vary between 14 and 66 mK km s^{-1} and are mainly sensitive to the line width. The 1_{10}–1_{01} ortho- and 1_{11}–0_{00} para-H_2O lines have similar integrated intensities, with line ratios 1_{10}–$1_{01}/1_{11}$–$0_{00} \sim 0.6$. The small variations in this ratio, caused by high opacities in the lines, makes these lines unfavorable as diagnostics.

Due to the rotation of the disk, the lines are broadened with increasing inclination, but at increasingly smaller integrated intensities because of the reduction of the apparent surface area of the disk. For a completely edge-on disk, absorption by the cold outer regions ($R \gtrsim 100$ AU) is important, but this effect has not been included in the present calculations. At an inclination of 60°, the rotational broadening extends to 5 km s^{-1} (best seen at $\delta v = 0.5$ km s^{-1}), which corresponds to a rotational velocity of $v_r = 10$ km s^{-1} or a radius of $R = 10$ AU. The dominant contributions to the 1_{10}–1_{01} line flux originate therefore from $R \gtrsim 10$ to 100 AU. Thus this line provides no information on the snow line, which is located close to the star, near $R \sim 1$ AU in this model (see Fig. 1).

At an inclination $i = 0°$ (face-on disk), the line width is determined by the turbulent velocity δv and the line opacity. The center of the line is strongly self-absorbed for no freezeout, since the emission produced at $N_H \sim 10^{22}$–10^{23} cm^{-2} is absorbed by the upper layers. These regions are subthermally excited because the densities are low ($n_H < 10^8$ cm^{-3}). Self-absorption occurs, but to a lesser extent, when freezeout is included and the residual water vapor abundance is $x_f(H_2O) = 10^{-8}$. Even for $x_f(H_2O) = 10^{-10}$, the line is still optically thick. For finite inclination angles, $i = 30°$ and 60°, flux loss at line center can also occur for the freezeout model with a water vapor abundance $x_f(H_2O) = 10^{-10}$. This is most clearly seen for the case $\delta v = 0.5$ km s^{-1}. This is not a signature of the snow line, since the flux loss occurs for $i = 60°$, for example, for velocities $v < 2$ km s^{-1}, corresponding to radii $R > 50$ AU.

Figure 3 illustrates the effects of noise on the line profile of the 1_{10}–1_{01} line. The sensitivity of the *Herschel* detectors at 1113.34 GHz is about 4 times less than at 556.936 GHz. According to the time estimator for the *Herschel Space Observatory*,[6] a 1 σ noise level of 0.5 and 2.0 mK can be obtained at the frequencies of the 1_{10}–1_{01} ortho and 1_{11}–0_{00} para transitions, respectively, in about 4 hr of observing time, when frequency switching is used and a spectral resolution of 1 km s^{-1} is requested. Thus the width, and to some degree the shape, of the 1_{10}–1_{01} ortho-H_2O line can be determined. However, the effect of self-absorption will be hard to distinguish for low turbulent velocities ($\delta v \leq 1.0$ km s^{-1}) at this resolution. The para line is not as a good candidate as the ortho transition for obtaining line shapes at the same noise level because of the decreased sensitivity.

The line profiles and integrated intensities of the 1_{10}–1_{01} and its ratio with the 1_{11}–0_{00} transition are affected by inclination angle, turbulent broadening, and the residual water vapor abun-

[5] See http://www.strw.leidenuniv.nl/WISH/.

[6] See http://herschel.esac.esa.int.

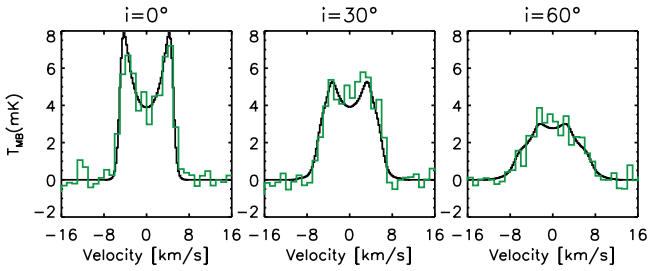

FIG. 3.—The 1_{10}–1_{01} ortho-H_2O line profile with a turbulent velocity of 2.0 km s^{-1} for inclinations (*left to right*) $i = 0°$, 30°, 60°, with freezeout and $x_f(H_2O) = 10^{-8}$. The model results are in black. For the curves in green, a 1 σ noise level of 0.5 mK has been added. The velocity resolution is assumed to be 1 km s^{-1}.

dance after freezeout. The dust opacity, which is influenced by grain growth and settling, can also play a role, although our study of these effects indicates that this is less important than the variables just mentioned. Thus the models are degenerate in the sense that different parameter sets give the same line shapes and intensities, due to the high opacities in these lines. Unfortunately, these are the only lines to be observed in the WISH program. Observing higher excitation transitions would help, but the decrease in sensitivity with frequency implies that only line fluxes and not line shapes can be determined. At a velocity resolution of 1 km s^{-1}, it would take *Herschel* about 4 hr to get the 1 σ noise level down to 2 mK for transition frequencies around ~1100 GHz. In a similar observation around ~1700 GHz, the noise level would be 8 mK.

Inspection of Table 1 shows that higher transitions may be observable with *Herschel*. We will now focus on the 3_{12}–3_{03} transition at 1097.37 GHz and the 2_{21}–2_{12} transition at 1661.01 GHz, although other lines may also have diagnostic value. Figure 4 plots the ratios of these two lines to the fundamental 1_{10}–1_{01} transition and shows that the ratios can distinguish between different levels of water vapor in the freezeout zone. The model results for no freezeout are found in the right upper part of the figure. Results for $x_f = 10^{-8}$ (*middle part*) and $x_f = 10^{-10}$ (*left lower part*) are clearly in a different region of the diagram and do not overlap with each other. The variations due to inclination and turbulent velocity are smaller than those associated with freezeout.

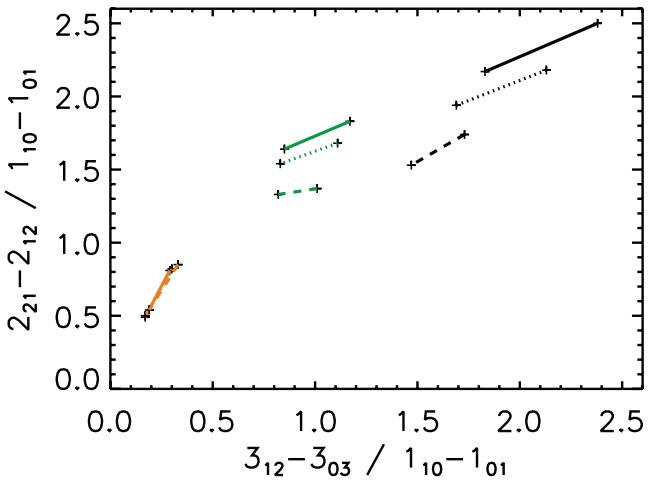

FIG. 4.—The 3_{12}–3_{03}/1_{10}–1_{01} vs. the 2_{21}–2_{12}/1_{10}–1_{01} ratio for models without freezeout (*black*), models with gas-phase abundances in the freezeout zone of $x_f(H_2O) = 10^{-8}$ (*green*) and 10^{-10} (*orange*). The different lines are for inclinations $i = 0°$ (*solid line*), 30° (*dotted line*), and 60° (*dashed line*).

4. CONCLUSIONS

We have shown that far-infrared rotational lines of water can be observed with the HIFI instrument on *Herschel*. These lines are produced in regions between radii $R \sim 10$–100 AU. The scheduled observations of the 1_{10}–1_{01} and 1_{11}–0_{00} transitions will probe the spatial distribution of water and the turbulence if the inclination of the disk is known. The ratios of these lines are quite similar for the different models (~0.6), due to the high opacities in both lines. The line shapes of the 1_{10}–1_{01} transition for different water vapor residuals in the freezeout zone are quite similar at the same inclination angle. Combining measurements of the 1_{10}–1_{01} line with higher transitions, such as the 3_{12}–3_{03} and 2_{21}–2_{12} lines, the abundance of the residual water vapor in the freezeout zone can be determined (see Fig. 4). These *Herschel* observations of rotational lines will complement observations of shorter wavelength excitation lines by *Spitzer* (10–20 μm; e.g., Carr & Najita 2008; Salyk et al. 2008), SOFIA (6 μm), and near-infrared rovibrational transitions (Carr et al. 2004; Salyk et al. 2008). These lines trace the inner regions of the disk out to radii $R \sim 1$–2 AU, with the potential of providing information on the conditions in the immediate neighborhood of the snow line.

This work has been supported by NSF grant AST 05-07423 and NASA grant NNG06GF88G to UC Berkeley. We thank F. van der Tak, P. d'Alessio, and the anonymous referee for their invaluable contributions.

REFERENCES

Boonman, A. M. S., et al. 2003, A&A, 406, 937
Carr, J. S., & Najita, J. R. 2008, Science, 319, 1504
Carr, J. S., Tokunaga, A. T., & Najita, J. 2004, ApJ, 603, 213
D'Alessio, P., Calvet, N., & Hartmann, L. 2001, ApJ, 553, 321
D'Alessio, P., Calvet, N., Hartmann, L., Lizano, S., & Cantó, J. 1999, ApJ, 527, 893
Davis, S. S. 2007, ApJ, 660, 1580
Dullemond, C. P., Hollenbach, D., Kamp, I., & D'Alessio, P. 2007, in Protostars and Planets V, ed. B. Reipurth, D. Jewitt, & K. Keil (Tucson: Univ. Arizona Press), 555
Faure, A., & Josselin, E. 2008, A&A, submitted
Fraser, H. J., Collings, M. P., McCoustra, M. R. S., & Williams, D. A. 2001, MNRAS, 327, 1165
Garaud, P., & Lin, D. N. C. 2007, ApJ, 654, 606
Glassgold, A. E., Najita, J., & Igea, J. 2004, ApJ, 615, 972
Hayashi, C. 1981, Prog. Theor. Phys. Suppl., 70, 35
Hogerheijde, M. R., & van der Tak, F. F. S. 2000, A&A, 362, 697
Jonkheid, B., Dullemond, C. P., Hogerheijde, M. R., & van Dishoeck, E. F. 2007, A&A, 463, 203
Jonkheid, B., Faas, F. G. A., van Zadelhoff, G.-J., & van Dishoeck, E. F. 2004, A&A, 428, 511
Kamp, I., & Dullemond, C. P. 2004, ApJ, 615, 991
Lecar, M., Podolak, M., Sasselov, D., & Chiang, E. 2006, ApJ, 640, 1115
Meijerink, R., Glassgold, A. E., & Najita, J. R. 2008, ApJ, 676, 518
Nomura, H., Aikawa, Y., Tsujimoto, M., Nakagawa, Y., & Millar, T. J. 2007, ApJ, 661, 334
Podolak, M., & Zucker, S. 2004, Meteoritics Planet. Sci., 39, 1859
Poelman, D. R., & Spaans, M. 2005, A&A, 440, 559
———. 2006, A&A, 453, 615
Salyk, C., et al. 2008, ApJ, 676, L49
Sasselov, D. D., & Lecar, M. 2000, ApJ, 528, 995
Schöier, F. L., van der Tak, F. F. S., van Dishoeck, E. F., & Black, J. H. 2005, A&A, 432, 369
Thi, W.-F., & Bik, A. 2005, A&A, 438, 557